Unraveling solvent and substituent effects in the photodynamics of light-dependent microtubule inhibitors for cancer phototherapy

Amirhossein Bakhtiiari[1] and Ruibin Liang[1]*

Correspondence to: Ruibin Liang (rliang@ttu.edu)

[1]Amirhossein Bakhtiiari

Department of Chemistry and Biochemistry, Texas Tech University, Lubbock, TX, 79409, USA

[1]Ruibin Liang

Department of Chemistry and Biochemistry, Texas Tech University, Lubbock, TX, 79409, USA

Abstract

In photopharmacology, molecular photoswitches enable light-controlled drug activities, offering precision in targeting biomolecular functions while minimizing side effects. Photostatins (PSTs) are photoswitchable analogs of combretastatin A-4 (CA4), designed to inhibit tubulin polymerization for cancer treatment. However, the influence of substituents and molecular environments on their photochemistry remains unclear. In this work, the *cis*-to-*trans* photodynamics of five PSTs (PST1 to PST5) in the vacuum and aqueous solution were simulated using the *ab initio* multiple spawning (AIMS) coupled with correlated multireference electronic structure calculations. Four distinct minima in the same conical intersection seam were discovered, serving as non-radiative decay channels. were discovered, serving as non-radiative decay channels. The aqueous environment slows photoisomerization and lowers its quantum yields, and changes the structures near the conical intersection seam. Substituent position and electronegativity significantly impact the isomerization kinetics by altering energy gaps between MECIs and the S_1 state at the Franck-Condon region. These findings provide useful insights into designing next-generation phototherapeutics for cancer.

Introduction

Photopharmacology offers a promising technique for achieving spatiotemporal and reversible control over biomolecular activities through light-matter interactions[1]. Its key advantage lies in using light to precisely and reversibly switch the isomer form of the photoswitchable ligands[2], which alters their interactions with the target biomolecules. As a result, it enables using illumination to reversibly activate and deactivate cell signaling and metabolic pathways in

precisely targeted regions, minimizing the side effects of traditional chemotherapeutics[3-7]. For instance, photostatins (PSTs) are a class of photoswitchable analogs of combretastatin A-4 (CA-4), a prominent inhibitor of microtubule polymerization that has progressed to clinical trials as tumor chemotherapeutics[8]. The photostationary state (PSS) under the illumination of ~400 nm wavelength light is dominated by the *cis* isomer form *(cis*-PST), which binds with high affinity at the colchicine pocket (lying at the interface between the two tubulin monomers) and inhibits their polymerization, triggering cell death[9]. The dark-adapted state or the PSS under ~510 nm light are dominated by the thermally more stable *trans*-PST, which has a much weaker binding affinity with tubulin than the *cis*-PST, triggering its unbinding from the target tubulin that restores the mitosis.[9] The photoisomerizations of the PSTs thus enabled reversible and precise control of the mitosis and death of tumor cells via light.[9]

Designing effective light-dependent drugs in photopharmacology requires careful optimization of several key factors[5]: (1) the binding affinity with the target biomolecule needs to be maximized in the active isomer form and minimized in the inactive isomer form, (2) the thermal relaxation time of the active isomer needs to be fine-tuned to meet the need of the treatment and to minimize its toxicity to the healthy cells in the un-illuminated areas, (3) the quantum yield of photoisomerization needs to be high to achieve quantitive, bidirectional switching between different isomers in PSS at different wavelengths[10]. Balancing these properties is critical for the development of promising phototherapeutic agents with high precision and minimal side effects[5,11].

Various photoswitchable analogs of CA-4 have been developed through chemical modifications of the PSTs[12-15], in addition to several successful designs based on the hemithioindigo (HTI) platform[16-18], different from the azobenzene-derived PSTs. However, it remains unclear, in general, how the chemical modifications on the photoswitches (Scheme 1) change their photochemical

reactivities, such as the kinetics and quantum yield of the photoisomerization. Also, it remains unclear how the molecular environment affects the kinetics and quantum yields of the photoswitches. A fundamental understanding of such structure-function relations at atomic-level details will improve their design in the future. To this end, here we aim to computationally investigate the photodynamics of five PST derivatives (PST1 to PST5), which are designed, synthesized and characterized previously[12], in the vacuum and aqueous solution.

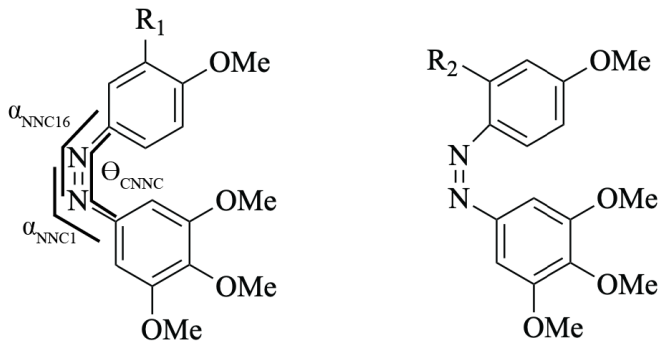

Photostatins (PSTs):

PST1: R1 (OH)
PST2: R1 (NH2)
PST3: R1 (F)
PST4: R2 (H)
PST5: R2 (F)

Scheme 1. Chemical structures of the five PSTs, i.e. PST1 to PST5, investigated in this study. The key carbon atoms (C16 and C1) near the central N=N double bond are labeled. The central torsion θ_{CNNC} and the bending angles α_{NNC16} and α_{NNC1} are labeled on the left panel.

Molecular simulations, with their ability to provide detailed insights into isomerization at the atomic level in a cost-effective manner, can bridge the gap between experimental observations and

the underlying mechanisms[19-24]. However, modeling photoisomerization reactions poses significant computational challenges because it is necessary to accurately describe the non-adiabatic dynamics across multiple electronic states, where the motion of electrons and nuclei are tightly coupled, but also the potential energy surfaces (PES) and non-adiabatic coupling of these states. Especially when the system approaches conical intersections and avoided crossings, where non-adiabatic transitions usually occur, the electronic wavefunctions often have a strong multireference nature, and it is important to use multireference QM methods to treat the static electron correlation properly.

In addition, substituents and molecular environment can modify the accessibility of conical intersection through geometrical influence, electronic effects, and topology modulation. For instance, bulky groups can hinder bond rotation or torsion, affecting the molecule's excited-state potential energy surfaces and the barriers of accessing certain regions of the CI seam. Additionally, the topography of the CI seam is influenced by the nature of the substituents. Some substituents may result in a perfectly peaked, hourglass-shaped CI, while others may lead to a more sloped CI along the branching planes. A sloped topography can reduce the quantum yield during photochemical processes[25].

To address these challenges, we employed the *ab initio* multiple spawning (AIMS) method[26-28] for performing non-adiabatic dynamics simulations, which are coupled with on-the-fly multireference electronic structure calculations using the hole-hole Tamm-Dancoff-Approximated density functional theory (hh-TDA-DFT)[29,30]. The hh-TDA-DFT method has been demonstrated by our research group for accurately and efficiently describing the ground and excited-state PESs of various molecular photoswitches (including azobenzene-derived ones) in complex molecular systems[20-24,31]. The original hh-TDA formalism utilized a double-anion

((N+2)-electrons) electronic configuration of the target N-electron system as the reference configuration. The annihilation of two electrons from this reference configuration as a response to the pairing field perturbation recovers the N-electron system. In the response process, both the ground and excited states of the original N-electron system are treated on equal footings as the excited state configurations of the (N+2)-electron reference configuration, and they are coupled together in the solution of eigenvalue problem derived from the response equations[29]. This is different from standard time-dependent DFT and configuration interaction singles (CIS), where typically the closed-shell ground-state configuration of the N-electron system is used as the reference configuration and decoupled from singly excited configurations due to Brillouin's theorem. Thus, the hh-TDA method can correctly describe the static correlation arising from the multireference character of the electron wavefunction near conical intersection and avoided crossings. An improved version of hh-TDA[30] eliminates the need to converge the molecular orbitals for the (N+2)-electron system and utilizes the floating occupation molecular orbital (FOMO) of the N-electron system to construct the (N+2)-electron reference configuration used in the eigenvalue problem. This improves the stability during the self-consistent field (SCF) convergence of molecular orbitals of the reference configuration.

Our AIMS simulation results identified four unique minima in the same conical intersection seam for all five PSTs, with population decay pathways closely correlated with the energy gaps between these MECIs and the S_1-state energy at the Franck-Condon region. The hh-TDA-DFT characterizations of these MECIs were further benchmarked using the extended multi-state complete active space second-order perturbation theory (XMS-CASPT2)[32-35], a highly accurate *ab initio* multireference electronic structure method. By influencing the excited-state dynamics towards these MECIs, the aqueous environment consistently slows down the rate and lowers the

quantum yields (QYs) of photoisomerization, with varying effects depending on the substituents. We will also discuss an appropriate computational protocol for sufficiently sampling the initial conditions (ICs) in order to generate unbiased results from the non-adiabatic dynamics simulations.

Methods

This section is divided into the following subsections: (1) system setup and classical molecular dynamics (MD) equilibration, (2) quantum mechanics/molecular mechanics (QM/MM) ground state MD equilibration, (3) AIMS simulations, and (4) benchmark calculations with the XMS-CASPT2[32-35] method.

System setup and classical MD equilibration

First, to construct the PST1, the CA-4 bound with tubulin was isolated from the crystal structure[36] (PDB code: 5LYJ). The central C=C double bond in CA-4 was converted into an N=N double bond linking two benzene rings, generating PST1. Next, the R group on one of the benzene rings (Scheme 1) was modified to generate the rest of the PST derivatives, i.e., PST2 to PST5.

For each of the five PSTs, the aqueous solution system was set up using the LEaP program in the AmberTools20 software package[37], solvating one PST molecule in a periodic boundary condition (PBC) simulation box of water molecules with 25×25×25 $Å^3$ dimension. The molecular mechanics (MM) force fields of the five PSTs were independently parameterized by the general AMBER force field (GAFF)[38,39] procedure, with special adjustments to the C-N=N-C and C-C-N=N torsions (θ_{CNNC} and θ_{CCNN}), which were not correctly captured by the default GAFF parameters

for the PSTs. These torsional terms in the force fields were fitted such that the relaxed scans of the PES along these reaction coordinates are consistent between the MM and the hh-TDA-BHHLYP/6-31G* Hamiltonians in terms of barrier heights and the relative energy difference between the ground-state energy minima of the *cis* and *trans* isomers (**Fig. S1**). This step is necessary to prevent artificially facile twisting of these torsions in the classical MD equilibration, which would otherwise occur using the default parameters obtained from the GAFF procedure. This setup ensured a relatively consistent Hamiltonian across all stages of MM and QM/MM equilibration, as well as during the post-AIMS, ground-state QM/MM simulations that tracked the ground-state dynamics after non-radiative decay. A zip file contains all the force fields parameters of the PST1, PT2, PST3, PST4, and PST5 are attached as part of the Supplementary Information. The water molecules in the aqueous solution system were treated with the SPC/Fw model[40].

For each aqueous solution system, firstly, the geometry was optimized over 25,000 steps, applying positional harmonic restraints with force constants of 100 kcal/mol/Å^2 to all non-hydrogen atoms of the PST. This minimization was followed by a 100 ps MD equilibration simulation in the constant NVT ensemble at 300 K temperature, without restraints on any atoms. Subsequently, a 200 ns production simulation was performed, in the constant NPT ensemble at 300 K temperature and 1 atm pressure, also without any restraints, to obtain 80 distinct snapshots for each system. These snapshots were evenly sampled with 1ns interval from the last part of the NPT production run, serving as starting points for QM/MM MD equilibration (see below). Throughout both the NVT and NPT MD simulations, the temperature and pressure (when applicable) were regulated using the Langevin thermostat (1 ps^{-1} collision frequency) and Berendsen barostat (2ps relaxation time), respectively. An integration timestep of 1 fs was used throughout the equilibration and

production simulations. The van der Waals interactions cutoff was 10 Å, and the particle-mesh Ewald method was used for calculating the electrostatic interactions.

Ground state QM/MM MD equilibration

For each snapshot extracted from the classical MD trajectories, an open-boundary subsystem of the original PBC system was built by extracting the PST molecule and all surrounding water molecules having at least one atom within 10 Å of any atoms of the PST molecule, generating 80 structures. This truncation accelerated the subsequent QM/MM equilibration and AIMS simulations. We conducted a ground state (S_0 state) QM/MM equilibration for each of the structures to sample various geometries near the Franck-Condon region of the *cis* minima. For each structure, we carried out a minimum of 2 ps of ground-state QM/MM equilibration at 300 K temperature using a timestep of 0.5 fs. The QM region contains the PST molecule, and the MM region contains the rest of the system. The electrostatic embedding scheme was used to couple the electronic density of the QM with the fixed-point charges of the MM regions.

The QM atoms were treated with the density functional theory using the BHHLYP functional with DFT-D3 dispersion correction[41] and the 6-31G* basis set (BHHLYP-D3/6-31G*), while the water molecules in the MM region were modeled using the SPF/Fw water model. The coordinates and velocities of all atoms in the final snapshots of the ground state QM/MM MD simulations constituted the initial conditions (ICs) of the AIMS simulations, totaling 400 ICs for the aqueous solution systems of all PSTs.

To explore the impact of the molecular environment on the photo-isomerization of the PSTs, we set up the PSTs in the vacuum using two methods. In method A, all water molecules were removed

in the final snapshot from the ground-state QM/MM simulations, generating 80 conformations of an isolated PST molecule for each of the 5 PSTs. Subsequently, each conformation was subject to equilibration with *ab initio* MD (AIMD) simulation at 300 K temperature for 2 ps, with the PST treated with the BHHLYP-D3/6-31G* method. The coordinates and velocities of the last snapshots of the 80 AIMD trajectories were chosen as the ICs. This approach enabled sufficient and balanced sampling of ICs near the *cis* isomer minima with the θ_{CNNC} spanning the range between ~ -15 to 15 degrees (see Results). In method B, a single AIMD trajectory of an isolated PST was propagated for 8 ps at 300K temperature, and 80 ICs were extracted with 100 fs interval. This method lacked sufficient sampling of the conformers residing near the FC region of the *cis* isomer (Results). In total, there were 800 ICs for AIMS simulations of five PSTs in the vacuum.

All ground state QM/MM MD equilibrations were performed using the TERACHEM[42-45] interfaced with OPENMM[46] packages. All AIMD equilibrations were performed using the TERACHEM software package.

Ab Initio Multiple Spawning (AIMS) simulation

For each system, 80 ICs were initiated on the S_1 electronic state, and the full multiple spawning (FMS) algorithm[26] was employed to simulate the non-adiabatic dynamics associated with the *cis* to *trans* photoisomerization. Briefly, during the AIMS simulation, the dynamics of the nuclear wavefunctions were represented as trajectory basis functions (TBF), which were propagated and expanded on the coupled potential energy surfaces of the S_0, S_1 and S_2 states following the FMS algorithm. The energies, gradients and non-adiabatic coupling of these three electronic states were calculated on-the-fly using QM/MM method, with the QM region treated with the hh-TDA-BHHLYP method for all systems. The QM atoms include the PST molecule only, and the MM

atoms include the rest of the system, i.e., all water molecules. The electrostatic embedding scheme was employed to describe the Coulomb interactions between the electronic density of the QM atoms with the fixed-point charges of the MM regions. During the AIMS algorithm, the QM/MM calculations are performed on the fly to provide the energies, gradients and non-adiabatic coupling of the system at each time step. The nuclear wave function was full-dimensional, including all nuclear degrees of the entire system. The nuclear wave function was represented as a linear combination of traveling Gaussian basis functions whose centers follow classical dynamics on their respective Born-Oppenheimer potential energy surface. They are referred to as trajectory basis functions (TBFs), which describe all translational, rotational, and vibrational degrees of freedom of the system. A 20 a.u. time step was used for integration during the AIMS simulation outside the spawning mode, while this time step was reduced into 5 a.u. in the spawning mode. To enter the spawning mode, the minimum threshold of 0.01 a.u. was employed to monitor the dot product between non-adiabatic coupling vector and the vector of all atoms' velocities.

For each IC, the AIMS simulation was terminated when more than 95% of the S_1 population had decayed to the S_0 state. The time evolution of the S_1 population decay was averaged over all ICs, and fitted to a first-order kinetics model (Eq 1):

$$P_{S_1}(t) = exp\,(-\frac{t}{\tau}), \qquad \text{Eq 1}$$

where t is the simulation time and τ is the relaxation time constant of the excited state.

The photoisomerization QYs was calculated by monitoring the final values of the θ_{CNNC} torsions of the S_0 TBFs' centroids. The trajectory was categorized as the *cis* isomer if the absolute value of the θ_{CNNC} was below 90 degrees, and *trans* isomer if above 90 degrees. The quantum yield was

calculated by dividing the total population of the S_0 TBFs ending up as the *trans* isomer with the total population of all S_0 TBFs. This method depended on the approximation that further propagating the S_0 TBFs on the ground state after the completion of the AIMS simulation did not lead to revisiting the region with strong non-adiabatic coupling or reverting the momentum of the θ_{CNNC} towards either the *cis* or *trans* isomer minimum. To test this approximation, for PST1, all ground-state TBFs were further propagated on the ground state for another 200 fs using hh-TDA-BHHLYP, followed by full minimization of the entire system and rechecking the θ_{CNNC} torsions of the PSTs with a tighter cutoff value (*cis* isomer: less than 30 degrees, *trans* isomer: greater than 150 degrees). The QYs calculated using this more rigorous and computationally expensive approach was identical to the more approximate and cheaper approach described above, thus validating the latter.

The error bars of the AIMS simulation results were estimated using bootstrapping of 1000 random samples for each set of 80 ICs. All AIMS simulations were performed using the FMS90 code interfaced with the TERACHEM/OPENMM software packages[42-46].

Benchmark calculations

In order to (1) benchmark the hh-TDA-BHHLYP method, and (2) interpret the trend of the photodynamics across the five PSTs, the minimum energy conical intersection (MECI) and the ground state (S_0 state) minima of the *cis* isomer for all five PSTs were optimized in the vacuum at both the hh-TDA-BHHLYP and XMS-CASPT2 levels of theory. First, we clustered the TBF centroid geometries at the $S_1 \rightarrow S_0$ spawning time during the AIMS simulations of PST4 in the vacuum (see Results). Starting from the representative snapshots of four unique clusters, the

S_0/S_1 MECIs of PST4 were optimized in the vacuum using the hh-TDA-BHHLYP-D3/6-31G* method. Then, the substituent R group was modified while keeping the coordinates of the rest of the molecule unchanged, generating the initial guess structures of the MECIs of PST1, PST2, PST3, and PST5. Afterwards, the four MECIs of each PSTs were optimized using the hh-TDA-BHHLYP/6-31G* method. The optimization of the ground-state *cis* isomer minima follows a similar procedure, except that the initial geometry of PST4 was taken from an equilibrated structure from the ground-state AIMD simulation in the vacuum.

The S_0/S_1 MECIs and *cis* isomer minima optimized at the hh-TDA-BHHLYP level of theory were further subject to optimizations at the XMS-CASPT2 level of theory. In the XMS-CASPT2 calculations, the reference wavefunctions were obtained from state-averaged complete active space self-consistent field (SA-CASSCF) calculations, which employed state-averaging of the lowest three singlet states (S_0, S_1 and S_2) and an active space of 10 electrons and 8 orbitals, consistent with our previous study[22]. This active space, used for constructing the SA-3-CASSCF(10e,8o) reference wavefunction, includes one lone pair orbital (n) localized on the nitrogen atoms and seven π orbitals. Figure S2 in the Supplementary Information (SI) illustrates the orbitals included in this active space. Furthermore, other previous studies demonstrated that the (10e,8o) active space is well-suited for describing the excited-state potential energy surfaces and MECIs of azobenzenes[30,47]. The XMS-CASPT2 calculations used an imaginary shift of 0.2 Hartree with no IPEA shift, and the cc-pVDZ basis set (i.e., XMS-CASPT2/SA-3-CASSCF(10e,8o)/cc-pVDZ).

All XMS-CASPT2 optimizations were performed using the BAGEL software package[48,49].

Comparing the topography of the minimum energy conical intersection in aqueous solution and vacuum

For each of the five PSTs in aqueous solution , we selected a spawning geometry sta with representative α_{NNC16} and α_{NNC1} values from the AIMS simulation, and optimized the MECI at the hh-TDA-BHHLYP/6-31G*/SPC/Fw level of theory in the same QM/MM settings as the AIMS. Subsequently, we isolated the PST and restarted the optimization of the MECI in the vacuum. We then calculated the following quantities of the MECIs in both the vacuum and the aqueous solution, using the definition introduced by Yarkony[50]:

$$\mathbf{g} = \frac{1}{2}\left(\frac{\partial E_1}{\partial \mathbf{R}} - \frac{\partial E_0}{\partial \mathbf{R}}\right) \quad \text{Eq 2}$$

$$\mathbf{h} = \left\langle \phi_1 \left| \frac{\partial H}{\partial \mathbf{R}} \right| \phi_0 \right\rangle \quad \text{Eq 3}$$

$$\mathbf{s} = \frac{1}{2}\left(\frac{\partial E_1}{\partial \mathbf{R}} + \frac{\partial E_0}{\partial \mathbf{R}}\right) \quad \text{Eq 4}$$

$$s^x = \frac{\mathbf{s} \cdot \mathbf{g}}{g^2} \quad \text{Eq 5}$$

$$s^y = \frac{\mathbf{s} \cdot \mathbf{h}}{h^2} \quad \text{Eq 6}$$

the E_0 and E_1 are the potential energies of the ground and first excited states, respectively. **g** is the difference of the gradient vectors between the S_0 and S_1 states. **h** is the nonadiabatic coupling vector between the two states. The *g* and *h* denote the norms of the **h** and **g** vectors, respectively. In Eq 4, **s** describes the average of the two gradient vectors of the two states. The s^x and s^y in Eqs 5-6 quantify the "slopedness" character of the MECIs. The larger absolute values of s^x and s^y indicate that the MECI is more sloped along the respective directions and can lead to less quantum yield[51].

Result and discussion

The primary goals of our simulations are to elucidate (1) the roles of substituents on the *cis*-*to*-*trans* photodynamics of the PST, (2) the effects of the aqueous environment on the mechanism of the photochemical reactions, and (3) an appropriate multiscale framework for sufficiently sampling the initial conditions (ICs) for obtaining reliable results from non-adiabatic dynamics simulations of molecular photoswitches. To achieve our goals, extensive *ab initio* non-adiabatic dynamics simulations were performed in this study to ensure the convergence of the results. In particular, for each of the five PSTs, AIMS simulations were performed starting from 80 ICs (coordinates and velocities of all the atoms) sampled near the ground-state *cis* isomer minima in both the aqueous solution and the vacuum, resulting in a total of 1200 AIMS simulations that propagated more than 2400 TBFs. In all AIMS simulations, the systems were initiated on the S_1 to simulate the nπ* photoexcitation, initiating the *cis*-to-*trans* photoisomerization.

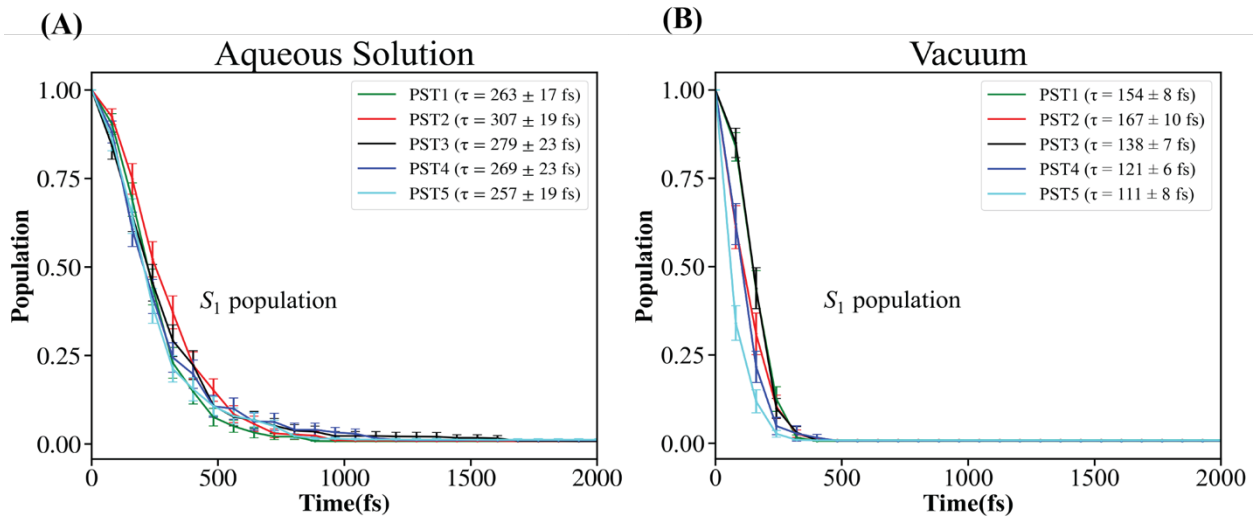

Figure 1. Decay of the S_1 population as a function of time after the nπ* excitation to the S_1 state during the *cis*-to-*trans* photoisomerization of the five PSTs (PST1 to PST5) in (A) aqueous solution and (B) the vacuum. The ICs for the AIMS simulations in the vacuum were prepared using method A Excited-state relaxation times constants for each PST are indicated on the legends

Table 1. Quantum yields (QY) for the *cis*-to-*trans* photoisomerization of the five PSTs (PST1-5) in the aqueous solution and vacuum.

Molecule	Aqueous solution	Vacuum
PST1	45 ± 4 %	48± 4 %
PST2	43 ± 4 %	50 ± 5 %
PST3	47 ± 4 %	53 ± 4 %
PST4	41 ± 4 %	57 ± 4 %
PST5	43 ± 4 %	46 ± 4 %

Effects of substituents on the non-radiative decay rates and quantum yields

The time evolution of the S_1 state population was extracted from the AIMS simulations and summarized in **Fig. 1 A & B**. The non-adiabatic relaxation time constants τ's, which are associated with the excited-state lifetime and isomerization rate, are summarized in the figures. The τ's for the five PSTs follow a relatively consistent trend in both environments. For instance, the τ's of PST2 and PST5 are the longest and shortest in both environments, respectively. The PST3 and PST5 only differ in the *ortho* vs. *meta* position of the fluorine substituent on the benzyl ring (Scheme 1), and the PST3 consistently has a longer excited-state lifetime than the PST5 in both environments. More generally, in both environments, the order of the τ's for PST2, PST3, PST4, and PST5 are the same: PST2>PST3>PST4>PST5. These results indicate that the substituents on the benzyl group of the PST (**Scheme 1**) influence the electronic properties of their excited states, as evidenced by differences in relaxation times. However, we admit that considering the uncertainties in the τ's, particularly for PST1, PST3 and PST4 in aqueous solution and PST1 and PST2 in the vacuum, these differences are not always statistically significant.

The QYs for the photoisomerization of five PSTs follow the order of PST4>PST3>PST2>PST1>PST5 in the vacuum and PST3>PST1$>$PST2$\approx$PST5>PST4 in the aqueous solution (Table 1). The difference between the highest and lowest QYs in the vacuum (PST4 vs. PST5) is beyond the statistical uncertainty, indicating non-negligible effects of substituents on the QYs. Interestingly, the order of the QYs is uncorrelated with the non-radiative decay rates (**Fig. 1**) in both environments, indicating complex dynamical effects influence the QY.

Effects of molecular environment on the non-radiative decay rates and quantum yields

The shift from the vacuum to the aqueous environment significantly increases the τ's and slows the population decay from the S_1 to S_0 state (**Fig. 1 A & B**). This trend is consistent for all five PSTs, with the largest difference in relaxation time observed for PST4 ($\Delta\tau = 148$ fs) and the smallest for PST1 ($\Delta\tau = 109$ fs). The relative ordering of the τ of PST1 with respect to other PSTs depends on the environment: it holds the 2nd place in the vacuum and 4th place in the aqueous solution. Notably, for PST1 in the aqueous solution, the simulated relaxation time constant ($\tau = 263 \pm 17\, fs$) agrees reasonably well with experiments[9,52] ($\tau = 250 fs$). The quantum yields are also decreased upon shifting from the vacuum to the aqueous environment (**Table 1**) for all five PSTs, with the largest difference observed for PST4 ($\Delta QY = 16$ %) and the smallest for PST1 and PST5 ($\Delta QY = 3$ %). The ordering of the QYs is also changed upon shifting the environment. In the vacuum, the PST4 and PST5 have the highest and lowest QYs, respectively. In contrast, in the aqueous solution, the PST3 and PST4 have the highest and lowest QYs, respectively (**Table 1**).

In the subsequent sections, we will explore the molecular origins of the observed differences in relaxation time constants and quantum yields between the two environments.

Characterization of minimum energy conical intersections in the vacuum

Understanding the impacts of substituents on the photoisomerization dynamics of the PSTs necessitates an in-depth characterization of the S_0/S_1 minimum energy conical intersections (MECIs). To this end, the MECIs mediating the non-adiabatic transitions from the S_1 to the S_0 state during the AIMS simulation were optimized in the vacuum. Specifically, the starting geometries

for the MECI optimizations were sampled by the centroids of S_0 TBFs at the $S_1 \rightarrow S_0$ spawning time in the AIMS simulations in the vacuum, which have large non-adiabatic coupling values. The optimized MECIs are clustered based on their central torsion θ_{CNNC}, and the two bending angles α_{NNC16} and α_{NNC1} (see Scheme 1 for definition). The four distinct types of MECIs for each PST are characterized as unique combinations of the θ_{CNNC} torsion and the two α_{CNN} angles. **Table 2** summarizes these key reaction coordinates of 4 unique minima along the CI seam and their relative energies with respect to the S_1 state energies at the ground-state *cis* isomer minimum. In addition, the structures of the four distinct MECI are compared to the corresponding structures at the *cis* minimum in **Fig. S6**. Both the MECI and S_0 minima were optimized at the hh-TDA-BHHLYP/6-31G* level of theory. The four types of MECIs all mediate non-radiative decay from excited populations in the AIMS simulations, but with different contributions (see **Table 2** and discussion below). Two of the MECIs feature θ_{CNNC} torsion near +90 degrees, and the other two near -90 degrees. Thus, it is evident that substituents influence the relative energies of the MECIs with respect to the S_1 energies in the FC region, which could elucidate the different relaxation time constants observed among the PSTs.

Table 2. Characterization of the four distinct S_0/S_1 MECIs of the five PSTs (PST1-5). For each type of PST, the energy (in kcal/mol) of each structure is reported as the relative energy with respect to the ground-state energy of the ground-state cis isomer minima for that PST. The S_1 state energies are reported for the *cis* minima.

Molecule	Properties	*cis* minima	MECI1	MECI2	MECI3	MECI4
PST1	Energy	82.67	45.73	39.95	48.47	39.88
	θ_{CNNC}	-3.95	89.74	90.20	-86.44	-90.77

	α_{NNC16}	120.90	116.62	139.86	116.38	137.29
	α_{NNC1}	124.48	148.61	117.16	146.20	117.28
PST2	Energy	83.87	50.71	44.99	51.15	45.38
	θ_{CNNC}	-3.77	88.19	90.02	-88.77	-90.40
	α_{NNC16}	120.75	116.73	140.45	116.32	140.29
	α_{NNC1}	123.81	147.27	117.16	145.94	116.99
PST3	Energy	84.72	51.01	43.76	48.72	42.68
	θ_{CNNC}	-5.17	90.74	89.85	-85.56	-90.58
	α_{NNC16}	120.83	116.67	139.61	116.52	135.81
	α_{NNC1}	122.94	147.38	117.16	147.76	117.11
PST4	Energy	84.15	53.50	46.52	50.83	48.40
	θ_{CNNC}	-4.11	82.14	90.62	-83.50	-91.09
	α_{NNC16}	120.73	116.38	138.37	116.29	137.51
	α_{NNC1}	124.00	146.60	117.18	147.99	117.77
PST5	Energy	94.16	50.85	46.09	52.25	46.46
	θ_{CNNC}	-5.85	82.94	89.43	-84.03	-89.52
	α_{NNC16}	119.04	115.87	139.04	115.91	139.84
	α_{NNC1}	120.68	145.43	116.84	145.21	116.94

The origin of the different relaxation time constants of the five PSTs in the vacuum

Fig. 2 displays a scatter plot of the geometries of the TBF centroids at $S_1 \rightarrow S_0$ spawning time, projected onto the 2D planes spanned by the α_{NNC16} angle and the θ_{CNNC} torsion. The radius of the circle at each point on the plot is proportional to the eventual population of the spawned TBF

on the ground state at the end of the AIMS simulation. To assess the impact of different substituents on the distribution, the scatter plot is divided into four sub-regions. Regions A and B feature a positive θ_{CNNC} torsion and an α_{NNC16} angle less than and greater than 125 degrees, respectively. Regions C and D feature a negative θ_{CNNC} torsion and an α_{NNC16} angle less than and greater than 125 degrees, respectively. The four regions A, B, C and D correspond to the vicinity of the MECIs 1, 2, 3 and 4 discussed above (**Table 1**), respectively. Following this, we calculated the percentages of $S_1 \rightarrow S_0$ population decay through each region. **Table 3** compares these percentages for PST2 and PST5, which have the longest and shortest relaxation time constants in the vacuum, respectively. The energy differences (ΔE) between the S_1 state at the Franck-Condon region and each type of MECI in the vacuum are also summarized. Both PST2 and PST5 predominantly decay through regions B and D due to the lower energies of MECIs 2 and 4 compared with MECIs 1 and 3 (**Table 3**).

Table 3. Percentage of the population transfer through the vicinity of each type of S_0/S_1MECI for PST2 and PST5, which have the highest and lowest relaxation time constants, respectively. For each PST, the energy differences ΔE's in (kcal/mol) between the S_1 state energy of the *cis* minimum and each MECI and the weighted-average ΔE over all four MECIs are summarized.

Molecule	MECI type	Percentage of population transfer	ΔE	Weight-averaged ΔE
PST2	MECI1	6.46%	33.16	38.18
	MECI2	63.95%	38.88	
	MECI3	3.63%	32.72	

	MECI4	25.96%	38.49	
PST5	MECI1	2.44%	43.31	46.93
	MECI2	36.41%	48.07	
	MECI3	13.68%	41.91	
	MECI4	47.47%	47.70	

Next, the ΔE's of the four types of MECIs in each PST was weight-averaged using the percentage of population decay through each type of MECI. The weight-averaged ΔE for PST2 is 38.18 kcal/mol, and for PST5, it is 46.93 kcal/mol. Based on this approximate analysis, we conclude that a greater difference in the energies of the S_1 state at the Franck-Condon region and the MECI correlates with faster non-radiative decay. Thus, the substituents influence the relative non-radiative decay rate by changing the energy difference between the FC point and the MECI on the excited state.

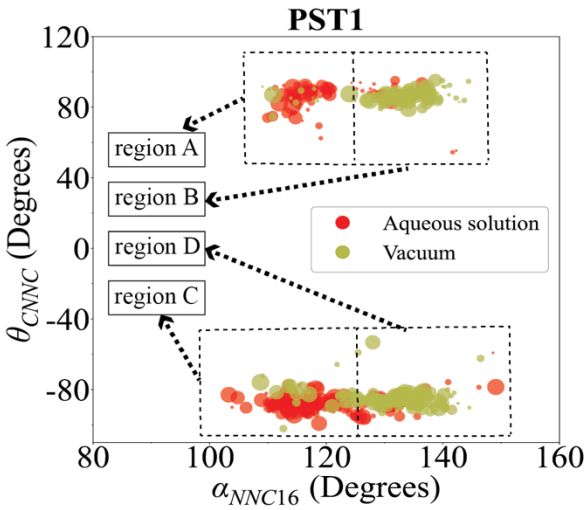
PST1
region A
region B
region D
region C
Aqueous solution
Vacuum
θ_{CNNC} (Degrees)
α_{NNC16} (Degrees)
120
80
40
0
-40
-80
80
100
120
140
160

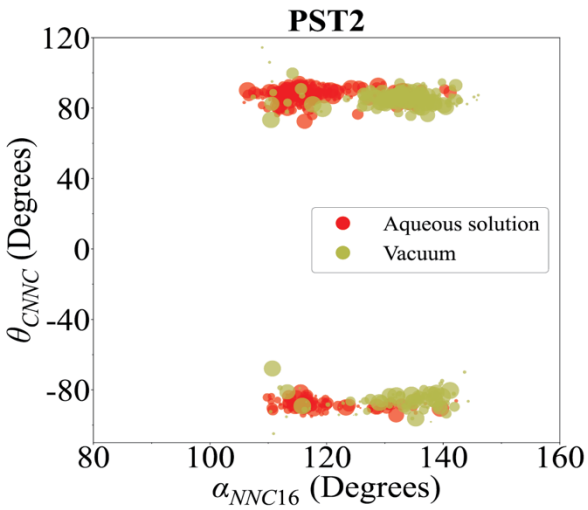
PST2
Aqueous solution
Vacuum
θ_{CNNC} (Degrees)
α_{NNC16} (Degrees)
120
80
40
0
-40
-80
80
100
120
140
160

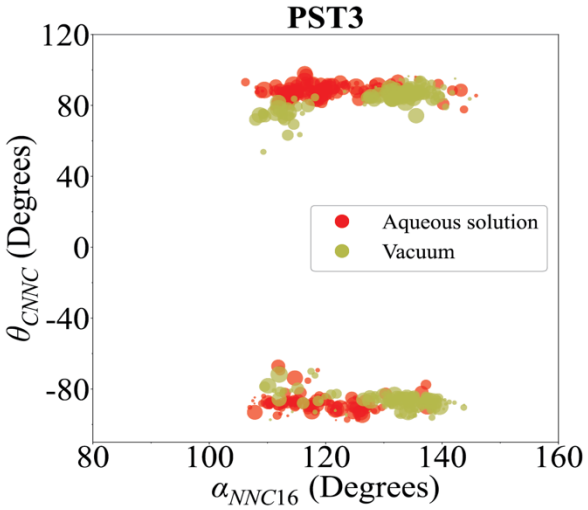
PST3
Aqueous solution
Vacuum
θ_{CNNC} (Degrees)
α_{NNC16} (Degrees)
120
80
40
0
-40
-80
80
100
120
140
160

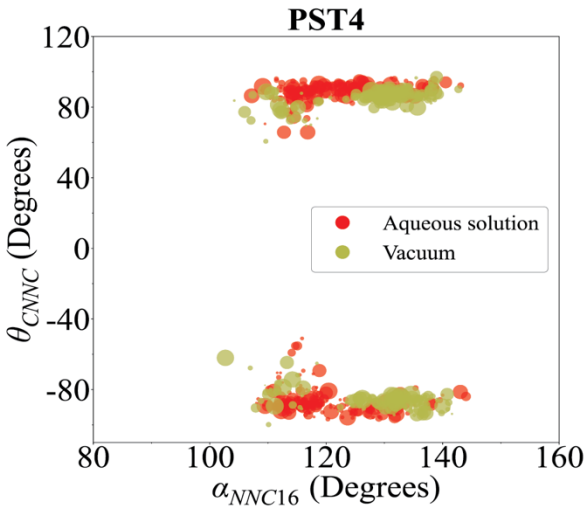
PST4
Aqueous solution
Vacuum
θ_{CNNC} (Degrees)
α_{NNC16} (Degrees)
120
80
40
0
-40
-80
80
100
120
140
160

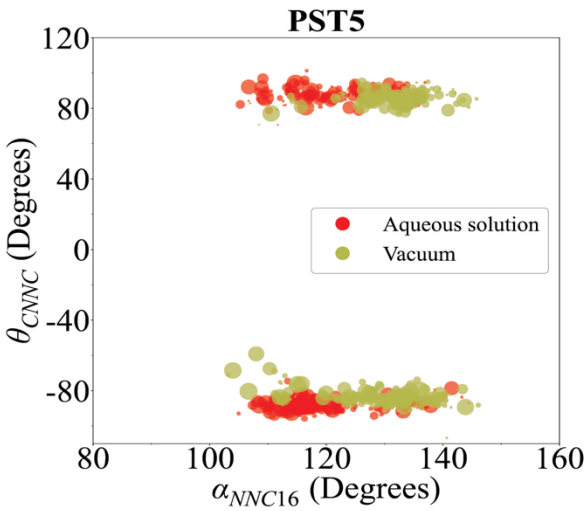
PST5
Aqueous solution
Vacuum
θ_{CNNC} (Degrees)
α_{NNC16} (Degrees)
120
80
40
0
-40
-80
80
100
120
140
160

Figure 2. Geometries of the TBF centroids at the $S_1 \rightarrow S_0$ spawning time points projected onto the 2D planes spanned by the θ_{CNNC} torsion and the α_{NNC16} angle. The radius of the circle around each point is proportional to the eventual population of the S_0 TBF. Data points in the vacuum and the aqueous solution are colored green and red, respectively. The four regions corresponding to the MECIs in Table 1 are also labeled in the panel of PST1.

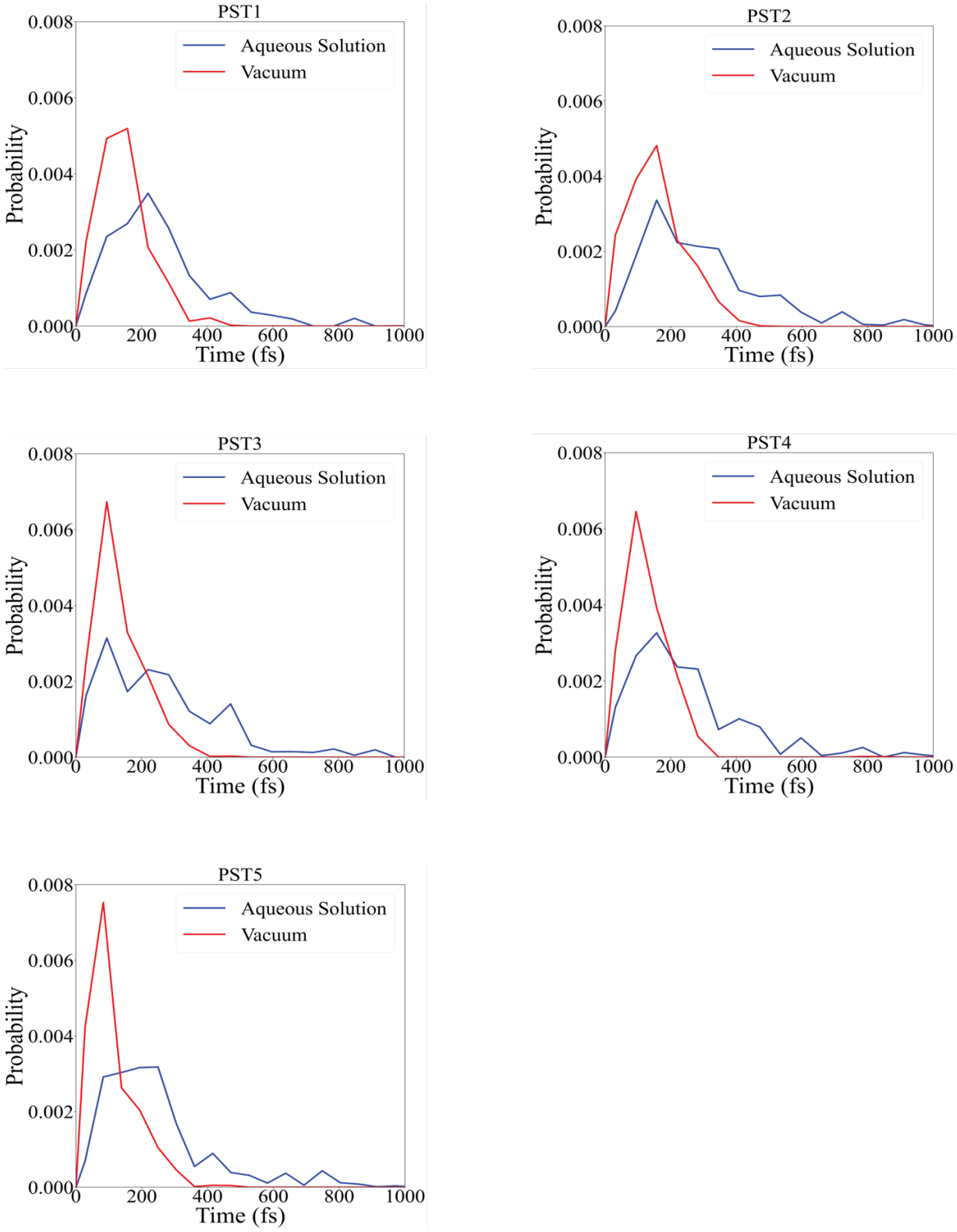

Figure 3. Probability distribution of the time of first spawning event in the AIMS simulations of PST1-5.

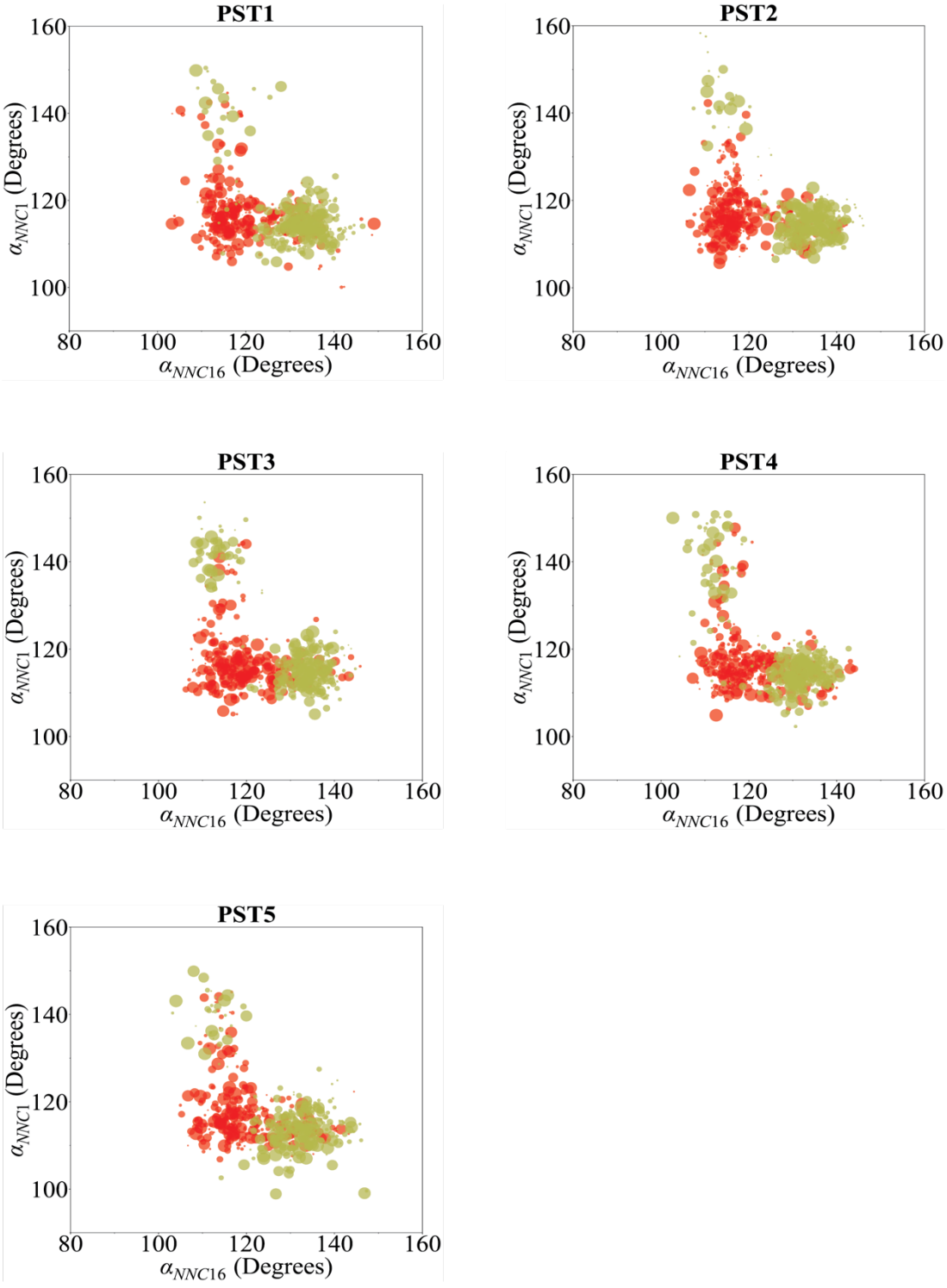

Figure 4. Geometries of the TBF centroids at the $S_1 \rightarrow S_0$ spawning time points projected onto the 2D planes spanned by the α_{NNC1} angle and the α_{NNC16} angle. The radius of the circle around

each point is proportional to the eventual population of the S_0 TBF. Data points in the vacuum and the aqueous solution are colored green and red, respectively.

Importantly, our results indicate that the polarity of the environment can influence the geometric details of the CI seam through which the excited-state population decays to the ground state. To illustrate this, we optimized the MECI structures in the aqueous solution at the hh-TDA-BHHLYP/6-31G*/SPC/Fw level of theory for all five PSTs, starting from spawning geometries with representative α_{NNC16} and α_{NNC1} values in **Fig. 4**. **Table 5** summarizes the optimized geometries, demonstrating how the aqueous solution adjusts both the α_{NNC16} and α_{NNC1} angles to approach similar values near 120 degrees. This contrasts with the vacuum, where the MECIs exhibit a larger difference between these two angles (Table 2), as was also found in a previous study[53] using CASSCF optimizations of the azobenzene molecule. The two MECIs with two different α_{CNN} bending angles when was found to belong to the same CI seam and are separated by a barrier due to angle bending in the CI seam space when the θ_{CNNC} is close to 90 degrees. In the aqueous solution, however, both our non-adiabatic dynamics trajectories and MECI optimization show that these two minima almost merge into one, and there is no significant α_{CNN} bending barrier separating them when θ_{CNNC} is close to 90 degrees, as evidenced. This new finding is significant, highlighting that the aqueous environment can reshape the PES in the conical intersection seam space and modify the barriers connecting the MECIs. In addition, we also compared the s^x parameters of the MECIs in the vacuum and aqueous solution (**Table 5,** see Method for definition**)**, as well as the branching planes representing the topography of the MECI in the aqueous solution and vacuum for PST2 (**Fig. 5**). The results indicate that changing to the aqueous environment from the vacuum is more likely to make the MECI more sloped (increase in the absolute value of s^x), thus reducing the quantum yield.

Table 5. Optimized geometries of PST1, PST2, PST3, PST4, and PST5 in Aqueous solution, along with the corresponding s^x value.

Molecule	θ_{CNNC}	α_{NNC16}	α_{NNC1}	s^x (Aqueous solution)	s^x (Vacuum)
PST1	-89.28	120.51	117.02	0.33	0.32
PST2	89.81	114.67	115.23	-1.55	-0.33
PST3	-88.63	119.90	115.14	-1.43	0.03
PST4	88.99	116.45	119.06	0.09	-0.28
PST5	-86.48	116.80	114.81	-1.09	-0.8

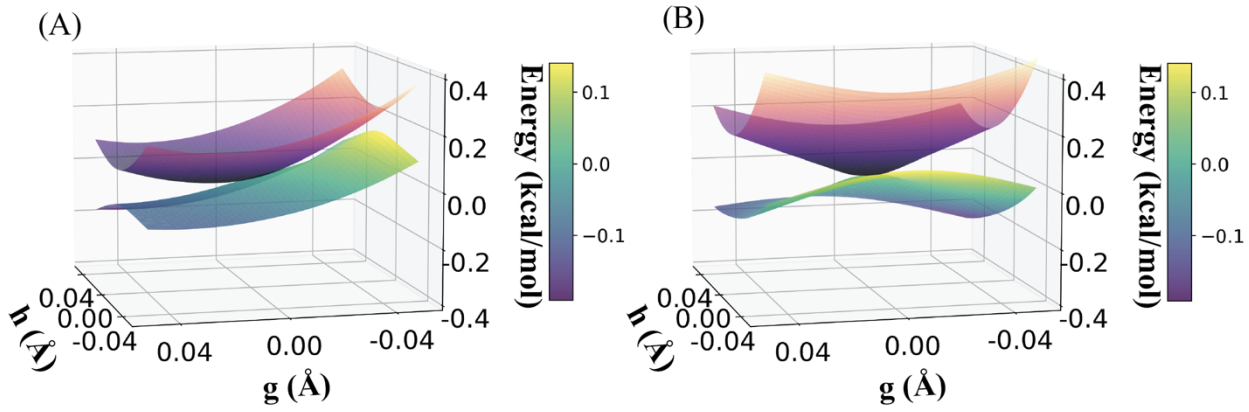

Figure 5. Topography of the S_0/S_1 MECI in (A) Aqueous solution and the (B) vacuum for PST2. In an aqueous solution, the topography of the CI is more sloped than that of the vacuum, which implies less quantum yield in the aqueous solution than the vacuum.

The origin of different non-radiative relaxation time constants and quantum yields between the two environments

The slower non-radiative decay rates in the aqueous solution can be attributed to the delayed access to the vicinity of the conical intersection seam on the S_1 state than in the vacuum. This effect from the environment is illustrated in **Fig. 3**, which compares the probability distribution of the time points at which the first spawning event occurred in the AIMS simulation starting from each IC. The results indicate that, on average, it takes longer for the PSTs to approaches the CI seam space in the aqueous solution than the vacuum. This is perhaps due to the steric and hydrogen bond interactions between the PST and the solvent molecules, which slow down the collective motion of the PST necessary for the θ_{CNNC} torsion to reach the values near +90 or -90 degrees.

The aqueous environment also modifies the non-radiative decay channel, which is reflected by the different $S_1 \rightarrow S_0$ spawning geometries in the two environments (**Fig. 4)**. In the aqueous solution, for all PSTs, the majority (averaged over five PSTs: 69.37%) of trajectories spawned within a limited range of 100 to 130 degrees for the α_{NNC1} angle and 90 to 125 degrees for the α_{NNC16} angle. In contrast, in the vacuum, the majority (averaged over five PSTs: 81.61%) of trajectories spawned within a range of 100 to 130 degrees for the α_{NNC1} angle and 125 to 150 degrees for the α_{NNC16} angle. Notably, the two separate clusters on the scatter plot in the vacuum (**Fig. 4**, green circles) are no longer distinguishable in the aqueous solution (**Fig. 4**, red circles). This comparison clearly illustrates the impact of the aqueous environment on shifting the location of the majority of non-adiabatic transition events.

As summarized in **Table 1**, shifting from the vacuum to the aqueous solution reduces the quantum yield for all PSTs. We attribute this effect to the influence of solvent molecules on the dynamics of PSTs near the non-adiabatic transition event. To investigate this, we analyzed the distribution of the velocity of the absolute value of the θ_{CNNC} torsion of the S_0 TBFs' centroids ($d|\theta_{CNNC}|/dt$) at the $S_1 \rightarrow S_0$ spawning time. In the velocity probability distribution calculations, the contribution to the histogram of velocities from each S_0 TBF is weighted by its final populations on the ground state. Such analysis was performed in both environments, and the distributions were further categorized based on whether the S_0 TBF ended up as the *cis* isomer reactant or the *trans* isomer photoproduct (**Fig. 6**). At the spawning time, the probability ratios of the torsional velocities being negative and positive are roughly the same in both environments (**Table S1**). However, in the *cis* isomer category of the distributions, the probability density for positive torsional velocity is higher

in the aqueous solution than in the vacuum (**Table S1**). In the *trans* isomer category of the distributions, the probability density for negative torsional velocity (less than -0.5 degrees/fs) is almost negligible in both environments. Thus, compared to the vacuum, in the aqueous solution, there is a higher likelihood of the θ_{CNNC} torsion reverting its isomerization trend towards the *trans* isomer photoproduct after the non-adiabatic transition to the S_0 state. The isomerization is more likely to be aborted on the ground state, yielding more *cis* isomer reactant and resulting in a lower quantum yield in the aqueous solution. This is because the aqueous environment slightly reduces the torsional mode's positive momentum when approaching the conical intersection seam space (**Fig. 6 A and B**, compare velocity distributions for *trans* isomer), which lowers the chance for the successful formation of the *trans* isomer photoproduct.

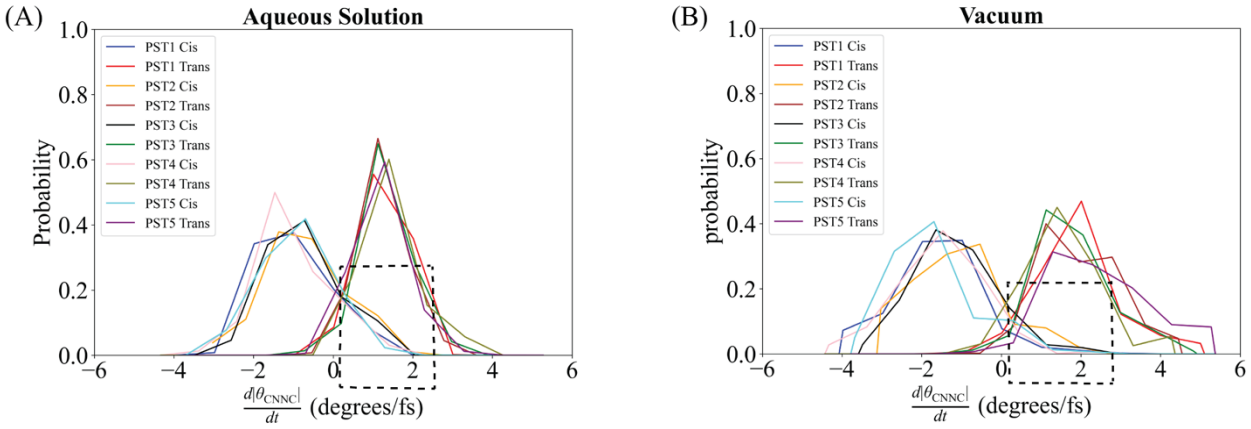

Figure 6. Probability distribution of the velocities of the absolute values of the θ_{CNNC} torsion at the $S_1 \rightarrow S_0$ spawning time of each S_0 TBF in (A) aqueous solution and (B) vacuum. The velocity probability distributions are weighted by the final populations of the S_0 TBFs. The distributions are categorized based on the type of isomer form into which each of the S_0 TBF eventually evolved.

The region corresponding to the isomerization being inverted on the ground state and yielding the *cis* isomer reactant are highlighted with dashed boxes.

Influences of IC sampling method on the AIMS results

To perform the AIMS simulations in the vacuum, we initially prepared the ICs employing ground-state AIMD simulations in the vacuum. Two methods were tested in this study. In the first method (Method A), the initial structures of the AIMD simulations were extracted from 80 independent ground-state QM/MM equilibration trajectories in the aqueous solution. The initial structures of these QM/MM trajectories, in turn, were sampled from the later part of a 200 ns classical MD production trajectory with intervals of 1 ns. Thus, the procedure of preparing the ICs in the vacuum has implicitly incorporated the conformational sampling from a 200 ns long classical MD trajectory. In the second method (Method B), we prepared the ICs by extracting coordinates and momenta with intervals of 100 fs from a short 8 ps AIMD trajectory at 300K temperature in the vacuum, starting from a ground-state *cis* isomer minimum. Interestingly, starting from the ICs prepared using Method B, during the AIMS simulations, for the PST1, PST3, PST4, and PST5, the motion of the θ_{CNNC} torsion is biased toward one direction. Almost all TBF spawning events occurred at either ~90 degrees (PST1, PST3, PST4) or ~-90 degrees (PST5), without a balanced sampling of pathways approaching all four types of MECIs **(Fig. 7)**. The lack of comprehensive reaction pathway sampling also leads to different S_1 state relaxation time constants and quantum yields, as well as the relative orders of these properties across the five PSTs (**Table 6 and Fig. S4**).

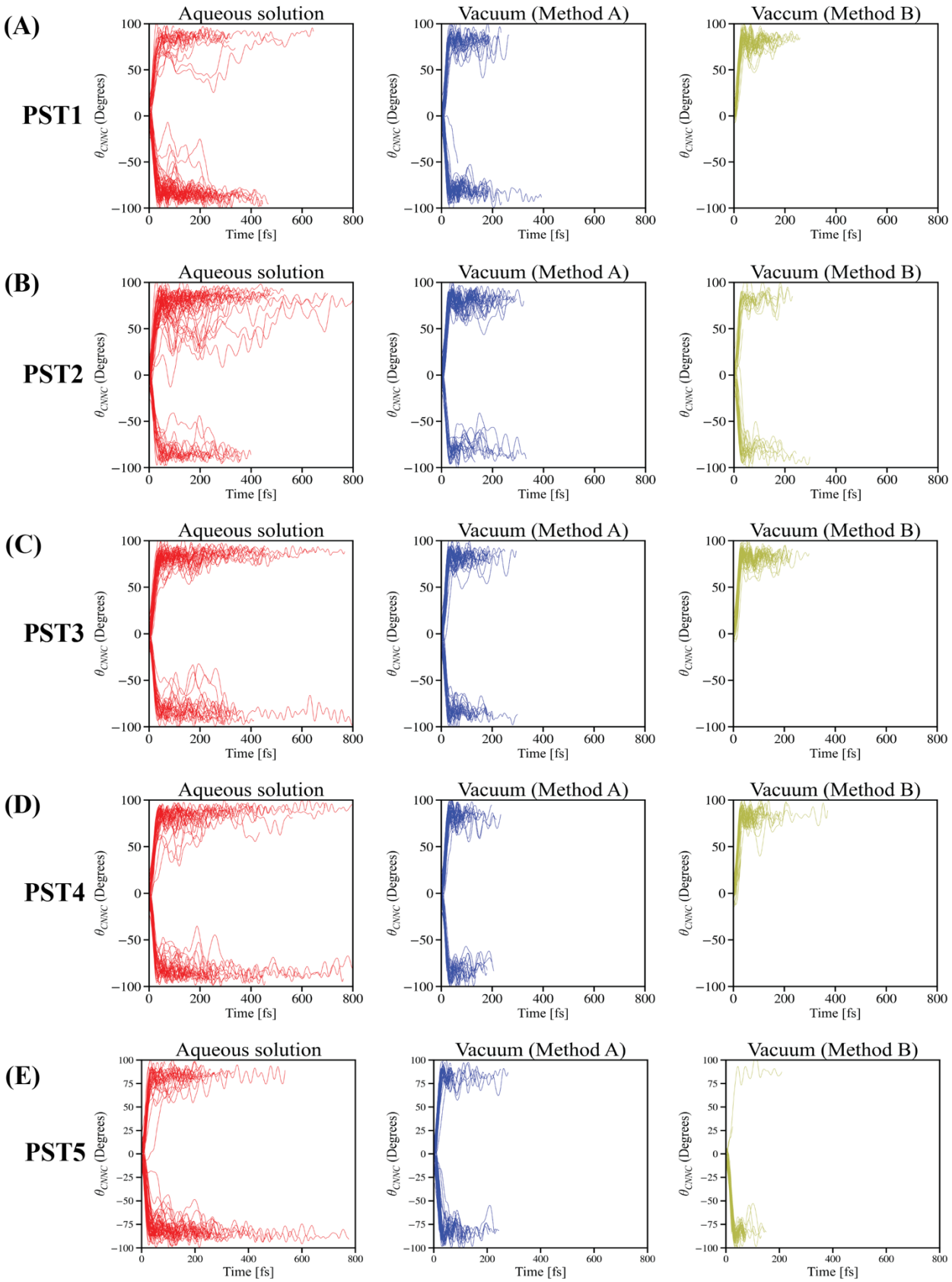
(A)
PST1
(B)
PST2
(C)
PST3
(D)
PST4
(E)
PST5
Aqueous solution
Vacuum (Method A)
Vaccum (Method B)
Vacuum (Method B)
θ_{CNNC} (Degrees)
Time [fs]

Figure 7. The comparison of the time evolution of the θ_{CNNC} torsion on the S_1 state before spawning to the ground state during AIMS simulations of (A) PST1, (B) PST2, (C) PST3, (D) PST4, and (E) PST5 in the aqueous solution and the vacuum. Different methods of preparing ICs (Methods A and B, see main text) result in different sampling of the non-radiative decay pathways.

Table 6. Comparison between the relaxation time constants (in fs) and quantum yields obtained from two sets of AIMS simulations in the vacuum. The ICs of these two sets of AIMS simulations were prepared with two different methods (see main text).

Molecule	Method A		Method B	
	Relaxation Time	QY	Relaxation Time	QY
PST1	154 ± 8	48 ± 4 %	162 ± 7	52 ± 5 %
PST2	167 ± 10	50 ± 5 %	132 ± 12	48 ± 5 %
PST3	138 ± 7	53 ± 4 %	163 ± 9	58 ± 5 %
PST4	121 ± 6	57 ± 4 %	120 ± 9	47 ± 6 %
PST5	111 ± 8	46 ± 4 %	92 ± 7	38 ± 5 %

These results highlight the need for a refined approach to preparing the ICs before initiating the non-adiabatic dynamics simulations. Even in the vacuum, it is crucial to sufficiently sample ICs from trajectories beyond the picosecond timescale in order to sample non-adiabatic decay pathways through various regions in the conical intersection seam. **Fig. S4** compares the distribution of the θ_{CNNC} torsion of the ICs prepared using different methods. In most cases, sampling the ICs in the vacuum from the equilibrated structures in an aqueous solution extracted

from an 80 ns long classical MD trajectory results in a more symmetric distributions of sampled θ_{CNNC} torsion around 0 degree. In contrast, sampling ICs from a single picosecond timescale AIMD trajectory in the vacuum results in asymmetric distributions of sampled θ_{CNNC} torsion, with a bias towards either positive or negative values that eventually translates to uneven sampling of the non-radiative decay pathways in the AIMS simulations. We believe this is caused by the existence of a small (~1-2 kcal/mol) but non-negligible energy barrier separating the two *cis* isomer minima with positive and negative values (~ ±10 degrees) θ_{CNNC} torsion. This barrier arises from steric repulsion between the two benzene rings when going from one *cis* minima to the other[22] (Fig S1 B). This small barrier makes Method B, with its short picosecond-scale sampling timescale, insufficient for converging the sampling of the two *cis* minima on the ground state. It is worth noting that this finding is consistent with a few recent studies[54-56] addressing the challenges for sampling ICs before starting non-adiabatic dynamics on the excited state, proposing solutions such as sampling on the ground state using thermostats or ensuring sufficiently long equilibration on the ground state before initiating excited-state dynamics[54-56]. The current study uniquely highlights the severity of this issue: it exists even for modest-sized systems in the vacuum with a few distinct shallow minima on the ground state, each generating very different non-radiative decay pathways during the photodynamics, and such sampling issues cannot be easily resolved by means of thermostats and picosecond-scale equilibration.

Benchmark calculations with the XMS-CASPT2 method

To benchmark the hh-TDA-BHHLYP method, we performed geometry optimizations of the ground-state *cis* isomer minima and the S_1/S_0 MECIs using the XMS-CASPT2/SA-3-CASSCF(10e,8o)/cc-pVDZ method (Method). As shown in **Table 7**, the order of the $S_0 \rightarrow S_1$

excitation energies at the *cis* isomer minima for the five PSTs are consistent between the hh-TDA-BHHLYP and the XMS-CASPT2 method (PST5>PST3>PST4>PST2>PST1). The optimized *cis* isomer minima using the two methods also align well (**Fig. S5**). Importantly, the existence of the four unique minima in the same CI seam for PST4 is confirmed through MECI optimizations using the XMS-CASPT2 method, with key reaction coordinates summarized in **Table 8**. Moreover, the structures of MECI1 for the five PSTs were re-optimized using the XMS-CASPT2 method, which also align reasonably well with the ones optimized using the hh-TDA-BHHLYP method (**Table 9**).

Table 7. The excitation energies (kcal/mol) from the S_0 to the S_1 state at the cis isomer minima for the five PSTs (PST1-5), which were optimized at either the hh-TDA-BHHLYP or XMS-CASPT2 levels of theory.

Molecule	Excitation energies	
	hh-TDA-BHHLYP	XMS-CASPT2
PST1	82.67	64.12
PST2	83.87	64.63
PST3	84.72	67.22
PST4	84.15	67.10
PST5	94.16	68.60

Table 8. The key torsion and angles (in degrees) of the four MECIs of PST4 optimized using the XMS-CASPT2 method.

Molecule	properties	MECI1	MECI2	MECI3	MECI4
PST4	θ_{CNNC}	91.16	91.57	-92.02	-92.69
	α_{NNC16}	116.52	138.36	116.07	138.37
	α_{NNC1}	134.06	115.78	135.97	116.19

Table 9. The comparison between the predicted key torsion and angles (in degrees) for the MECI1 optimized using the hh-TDA-BHHLYP and XMS-CASPT2 methods. All the angles and dihedrals are in degrees.

PST derivatives	Method	Reaction coordinates (degrees)		
		θ_{CNNC}	α_{NNC16}	α_{NNC1}
PST1	hh-TDA-BHHLYP	89.74	116.62	148.61
	XMS-CASPT2	91.4	116.47	134.87
PST2	hh-TDA-BHHLYP	88.19	116.73	147.27
	XMS-CASPT2	92.25	116.25	136.01
PST3	hh-TDA-BHHLYP	90.74	116.67	147.38
	XMS-CASPT2	92.22	116.21	136.39
PST4	hh-TDA-BHHLYP	82.14	116.38	146.6
	XMS-CASPT2	91.16	116.52	134.06
PST5	hh-TDA-BHHLYP	82.94	115.87	145.43
	XMS-CASPT2	95.18	118.42	137.15

Conclusions

In summary, employing AIMS simulation coupled with on-the-fly correlated multireference electronic structure calculations, we systematically characterized the effect of substituents and molecular environment on the *cis*-to-*trans* photodynamics of a series of PST derivatives in both the vacuum and the aqueous solution. The aqueous environment slows down the speed by which the conical intersection is approached from the *cis* isomer's FC region on the S_1 state, thus elongating the excited-state lifetime compared to the vacuum. The quantum yield is also reduced in the aqueous environment due to the lower momentum of the isomerizing dihedral at non-adiabatic transition. Four distinct MECIs were observed to mediate the *cis* to *trans* photodynamics of all PSTs in the vacuum. However, in the aqueous solution, the non-radiative decay channels were more concentrated without a clear pattern of separation based on the four MECIs. The substituents have an obvious impact on the kinetics but not on the quantum yields of photoisomerization. The isomerization rate is positively related to the energy gap between the S1 state's energy and the MECI energy in the vacuum.

Furthermore, two sampling protocols were compared for preparing the initial conditions (ICs) of the non-adiabatic dynamics simulation, which elucidates that insufficient IC sampling from a single picosecond timescale ground-state *ab initio* molecular dynamics trajectory can generate biased results from non-adiabatic dynamics simulations even in the simplest molecular environment, i.e., the vacuum. Such observations are key for establishing a correct computational protocol for simulating the photodynamics of molecular photoswitches in complex biomolecular environments.

Supplemental information

The supplemental information contains Figures S1-S6. They include the active space orbitals, PES scan using the hh-TDA-BHHLYP and MM force field, time evolution of S_1 population of the PSTs in the vacuum using the IC sampled by Method B, distributions of the θ_{CNNC} torsion of the ICs prepared in different environments and methods, comparison of the *cis* isomer minima optimized by the XMS-CASPT2 and hh-TDA-BHHLYP methods, and comparison of *cis* isomer minima with MECIs. It also includes Table S1 for quantitative analysis of ground-state backward isomerization, as well as the cartesian coordinates (in XYZ file format) of the *cis* minima and MECIs optimized by the hh-TDA-BHHLYP and XMS-CASPT2 methods.

Acknowledgments

Ruibin Liang acknowledges the grant support from the Robert A. Welch Foundation (grant number: D-2108-20220331). We also acknowledge the computing facilities provided by the High-Performance Computing Center at Texas Tech University.

Keywords: non-adiabatic dynamics, multireference quantum chemistry methods, conical intersection, cancer phototherapy, drug design

References

1. Hüll, K.; Morstein, J.; Trauner, D. Chem Rev 2018, 118(21), 10710-10747.
2. Szymanski, W.; Beierle, J. M.; Kistemaker, H. A.; Velema, W. A.; Feringa, B. L. Chemical reviews 2013, 113(8), 6114-6178.
3. Broichhagen, J.; Frank, J. A.; Trauner, D. Acc Chem Res 2015, 48(7), 1947-1960.
4. Kazim, M.; Yoo, E. Angewandte Chemie 2024, 136(2), e202310694.
5. Kobauri, P.; Dekker, F. J.; Szymanski, W.; Feringa, B. L. Angewandte Chemie International Edition 2023, 62(30), e202300681.

6. Sahoo, J.; Sahoo, S.; Subramaniam, Y.; Bhatt, P.; Rana, S.; De, M. Angewandte Chemie 2024, 136(1), e202314804.
7. Liu, R.; Yao, J.; Zhou, S.; Yang, J.; Zhang, Y.; Yang, X.; Li, L.; Zhang, Y.; Zhuang, Y.; Yang, Y. Nature Protocols 2024, 19(2), 374-405.
8. Pettit, G. R.; Singh, S. B.; Hamel, E.; Lin, C. M.; Alberts, D. S.; Garcia-Kendal, D. Experientia 1989, 45(2), 209-211.
9. Borowiak, M.; Nahaboo, W.; Reynders, M.; Nekolla, K.; Jalinot, P.; Hasserodt, J.; Rehberg, M.; Delattre, M.; Zahler, S.; Vollmar, A.; Trauner, D.; Thorn-Seshold, O. Cell 2015, 162(2), 403-411.
10. Stranius, K.; Börjesson, K. Scientific reports 2017, 7(1), 1-9.
11. Rastogi, S. K.; Zhao, Z.; Barrett, S. L.; Shelton, S. D.; Zafferani, M.; Anderson, H. E.; Blumenthal, M. O.; Jones, L. R.; Wang, L.; Li, X. European journal of medicinal chemistry 2018, 143, 1-7.
12. Borowiak, M.; Nahaboo, W.; Reynders, M.; Nekolla, K.; Jalinot, P.; Hasserodt, J.; Rehberg, M.; Delattre, M.; Zahler, S.; Vollmar, A. Cell 2015, 162(2), 403-411.
13. Engdahl, A. J.; Torres, E. A.; Lock, S. E.; Engdahl, T. B.; Mertz, P. S.; Streu, C. N. Organic letters 2015, 17(18), 4546-4549.
14. Rastogi, S. K.; Zhao, Z.; Barrett, S. L.; Shelton, S. D.; Zafferani, M.; Anderson, H. E.; Blumenthal, M. O.; Jones, L. R.; Wang, L.; Li, X.; Streu, C. N.; Du, L.; Brittain, W. J. Eur J Med Chem 2018, 143, 1-7.
15. Sheldon, J. E.; Dcona, M. M.; Lyons, C. E.; Hackett, J. C.; Hartman, M. C. T. Org Biomol Chem 2016, 14(1), 40-49.
16. Sailer, A.; Ermer, F.; Kraus, Y.; Lutter, F. H.; Donau, C.; Bremerich, M.; Ahlfeld, J.; Thorn-Seshold, O. Chembiochem 2019, 20(10), 1305-1314.
17. Sailer, A.; Ermer, F.; Kraus, Y.; Bingham, R.; Lutter, F. H.; Ahlfeld, J.; Thorn-Seshold, O. Beilstein J Org Chem 2020, 16, 125-134.
18. Sailer, A.; Meiring, J. C. M.; Heise, C.; Pettersson, L. N.; Akhmanova, A.; Thorn-Seshold, J.; Thorn-Seshold, O. Angew Chem Int 2021, 60(44), 23695-23704.
19. Ryazantsev, M. N.; Strashkov, D. M.; Nikolaev, D. M.; Shtyrov, A. A.; Panov, M. S. Russian Chemical Reviews 2021, 90(7), 868.
20. Liang, R.; Bakhtiiari, A. J Chem Phys 2022, 156(24), 245102.
21. Liang, R.; Bakhtiiari, A. J Phys Chem B 2022, 126(12), 2382-2393.
22. Bakhtiiari, A.; Costa, G. J.; Liang, R. J Chem Theory Comput 2023, 19(18), 6484-6499.
23. Liang, R. J Chem Theory Comput 2021, 17(5), 3019-3030.
24. Liang, R.; Das, D.; Bakhtiiari, A. Phys Chem Chem Phys 2021, 23(46), 26263-26272.
25. Blancafort, L. ChemPhysChem 2014, 15(15), 3166-3181.
26. Ben-Nun, M.; Quenneville, J.; Martínez, T. J. J Phys Chem A 2000, 104(22), 5161-5175.
27. Curchod, B. F. E.; Martínez, T. J. Chem Rev 2018, 118(7), 3305-3336.
28. Ben-Nun, M.; Martínez, T. J. In Adv Chem Phys; John Wiley & Sons, Inc., 2002, p 439-512.
29. Bannwarth, C.; Yu, J. K.; Hohenstein, E. G.; Martínez, T. J. J Chem Phys 2020, 153(2), 024110.
30. Yu, J. K.; Bannwarth, C.; Hohenstein, E. G.; Martínez, T. J. Journal of Chemical Theory and Computation 2020, 16(9), 5499-5511.
31. Yu, J. K.; Bannwarth, C.; Liang, R.; Hohenstein, E. G.; Martínez, T. J. J Am Chem Soc 2020, 142(49), 20680-20690.

32. Shiozaki, T.; Győrffy, W.; Celani, P.; Werner, H.-J. J Chem Phys 2011, 135(8), 081106.
33. Finley, J.; Malmqvist, P.-Å.; Roos, B. O.; Serrano-Andrés, L. Chem Phys Lett 1998, 288(2), 299-306.
34. Andersson, K.; Malmqvist, P. Å.; Roos, B. O. J Chem Phys 1992, 96(2), 1218-1226.
35. Andersson, K.; Malmqvist, P. A.; Roos, B. O.; Sadlej, A. J.; Wolinski, K. J Phys Chem 1990, 94(14), 5483-5488.
36. Gaspari, R.; Prota, A. E.; Bargsten, K.; Cavalli, A.; Steinmetz, M. O. Chem 2017, 2(1), 102-113.
37. Case, D. A.; Aktulga, H. M.; Belfon, K.; Ben-Shalom, I. Y.; Brozell, S. R.; Cerutti, D. S.; Cheatham, I., T.E; Cruzeiro, V. W. D.; Darden, T. A.; Duke, R. E.; Giambasu, G.; Gilson, M. K.; Gohlke, H.; Goetz, A. W.; Harris, R.; Izadi, S.; Izmailov, S. A.; Jin, C.; Kasavajhala, K.; Kaymak, M. C.; King, E.; Kovalenko, A.; Kurtzman, T.; Lee, T. S.; LeGrand, S.; Li, P.; Lin, C.; Liu, J.; Luchko, T.; Luo, R.; Machado, M.; Man, V.; Manathunga, M.; Merz, K. M.; Miao, Y.; Mikhailovskii, O.; Monard, G.; Nguyen, H.; O'Hearn, K. A.; Onufriev, A.; Pan, F.; Pantano, S.; Qi, R.; Rahnamoun, A.; Roe, D. R.; Roitberg, A.; Sagui, C.; Schott-Verdugo, S.; Shen, J.; Simmerling, C. L.; Skrynnikov, N. R.; Smith, J.; Swails, J.; Walker, R. C.; Wang, J.; Wei, H.; Wolf, R. M.; Wu, X.; Xue, Y.; York, D. M.; Zhao, S.; Kollman, P. A.: University of California, San Francisco. , 2021.
38. Wang, J.; Wolf, R. M.; Caldwell, J. W.; Kollman, P. A.; Case, D. A. J Comput Chem 2004, 25(9), 1157-1174.
39. Wang, J.; Wang, W.; Kollman, P. A.; Case, D. A. J Mol Graph Model 2006, 25(2), 247-260.
40. Wu, Y. J.; Tepper, H. L.; Voth, G. A. J Chem Phys 2006, 124(2).
41. Grimme, S.; Antony, J.; Ehrlich, S.; Krieg, H. J Chem Phys 2010, 132(15).
42. Ufimtsev, I. S.; Martinez, T. J. J Chem Theory Comput 2009, 5, 2619-2628.
43. Titov, A. V.; Ufimtsev, I. S.; Luehr, N.; Martinez, T. J. J Chem Theory Comput 2013, 9, 213-221.
44. Seritan, S.; Bannwarth, C.; Fales, B. S.; Hohenstein, E. G.; Kokkila-Schumacher, S. I. L.; Luehr, N.; Snyder, J. W.; Song, C.; Titov, A. V.; Ufimtsev, I. S.; Martinez, T. J. J Chem Phys 2020, 152, 224110.
45. Seritan, S.; Bannwarth, C.; Fales, B. S.; Hohenstein, E. G.; Isborn, C. M.; Kokkila-Schumacher, S. I. L.; Li, X.; Liu, F.; Luehr, N.; Snyder, J. W.; Song, C.; Titov, A. V.; Ufimtsev, I. S.; Wang, L.-P.; Martinez, T. J. Wiley Interdisciplinary Reviews: Computational Molecular Science 2020, e1494.
46. Eastman, P.; Friedrichs, M. S.; Chodera, J. D.; Radmer, R. J.; Bruns, C. M.; Ku, J. P.; Beauchamp, K. A.; Lane, T. J.; Wang, L.-P.; Shukla, D.; Tye, T.; Houston, M.; Stich, T.; Klein, C.; Shirts, M. R.; Pande, V. S. J Chem Theory Comput 2013, 9(1), 461-469.
47. Casellas, J.; Bearpark, M. J.; Reguero, M. ChemPhysChem 2016, 17(19), 3068-3079.
48. Shiozaki, T. WIREs Computational Molecular Science 2018, 8(1), e1331.
49. Shiozaki, T.
50. Yarkony, D. R. J Chem Phys 2001, 114(6), 2601-2613.
51. Liu, L.; Liu, J.; Martinez, T. J. The Journal of Physical Chemistry B 2016, 120(8), 1940-1949.
52. Standfuss, J.; Weinert, T.; Wranik, M.; Church, J.; Seidel, H. P.; Slavov, C.; Masini, T.; James, D.; Glover, H.; Carrillo, M. Research Square 2023, PREPRINT (Version 1)
53. Conti, I.; Garavelli, M.; Orlandi, G. J Am Chem Soc 2008, 130(15), 5216-5230.

54. Suchan, J.; Hollas, D.; Curchod, B. F.; Slavíček, P. Faraday discussions 2018, 212, 307-330.
55. Curtis, E.; Jones, C.; Martinez, T. 2024.
56. Avagliano, D.; Lorini, E.; González, L. Philosophical Transactions of the Royal Society A 2022, 380(2223), 20200381.

Table of Contents Graphics

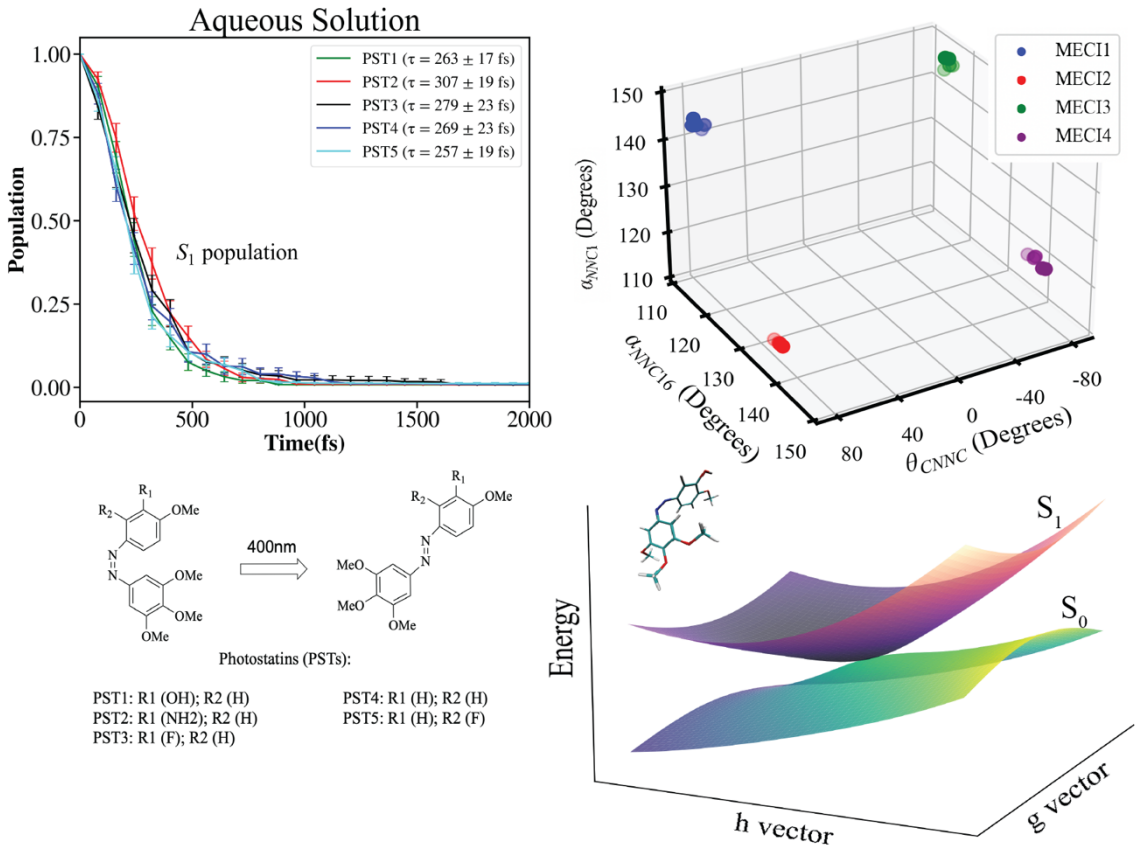

Short Summary

The effects of substituents and solvent effects on the *cis*-to-*trans* photodynamics of five derivatives of photostatin, a promising class of light-regulated therapeutics for cancer treatment, are systematically investigated using accurate *ab initio* non-adiabatic dynamics simulations coupled with on-the-fly correlated electronic structure calculations. Four unique minima in the same CI seam between the S_0 and S_1 states were identified for mediating the non-radiative decay, which was confirmed by XMS-CASPT2 calculations.